

**NASA CONTRACTOR
REPORT**

NASA CR-44

44P



296
NASA CR-44

(Revised,
July 1964)

N64-24825

100-1

009

PYROELECTRIC DETECTION TECHNIQUES AND MATERIALS

Prepared under Contract No. NASw-711 by
SPERRY MICROWAVE ELECTRONICS COMPANY
Division of Sperry Rand Corporation
Clearwater, Florida

for

NASA CR-44

NOTICE

This revised copy replaces the
previously distributed copy.
Please destroy copies originally
issued under date of April 1964.

PYROELECTRIC DETECTION TECHNIQUES AND MATERIALS

Prepared under Contract No. NASw-711 by
SPERRY MICROWAVE ELECTRONICS COMPANY
Division of Sperry Rand Corporation
Clearwater, Florida

This report is reproduced photographically
from copy supplied by the contractor.

NATIONAL AERONAUTICS AND SPACE ADMINISTRATION

For sale by the Office of Technical Services, Department of Commerce,
Washington, D.C. 20230 -- Price \$1.25

TABLE OF CONTENTS

FACTUAL DATA	1
Equivalent Circuit Considerations	1
Square Wave Analysis	8
Materials Preparation	9
Measurement Apparatus	13
Experimental Results	16
CONCLUSIONS AND RECOMMENDATIONS	27
Summary of Results	27
Applications of the Pyroelectric Technique	29
Recommendations	32
APPENDIX A Solution of Heat Equation for Sinusoidal Modulation	A-1
APPENDIX B $T^*(t)$ for Square Wave Modulation	B-1
APPENDIX C Signal Voltage for Square Wave Modulation	C-1

FACTUAL DATA

EQUIVALENT CIRCUIT CONSIDERATIONS

Introduction

A theoretical expression for NEP (noise equivalent power) has been obtained using a sinusoidal source of energy and assuming parameters in the equivalent circuit to be linear elements. The equivalent circuit was expressed in terms of an ideal voltage generator. Because it is somewhat more informative, an ideal current generator representation of the equivalent circuit is used in this report.

The analysis for sinusoidal modulation is reviewed and extended and the analysis for square wave modulation is given.

Sinusoidal Modulation

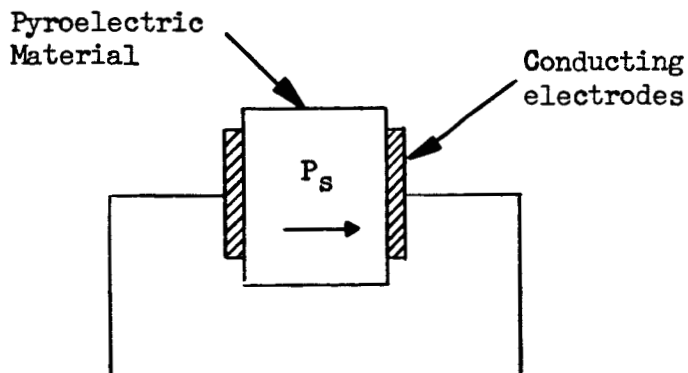


Figure 1. Representation of a pyroelectric detector crystal.

Figure 1 depicts a spontaneously polarized material with electrodes of area A on the faces, forming a capacitor C_x with conductance G_x . To a good approximation, the current through the material is given by

$$i = G_x V_b + \frac{d}{dt} (C_x V_b + A P_s), \quad (1)$$

where

i = current into the sample

G_x = conductance of the sample

V_b = voltage across the sample

C_x = capacitance of the sample

P_s = space average of the spontaneous polarization of the sample

A = area of sample,

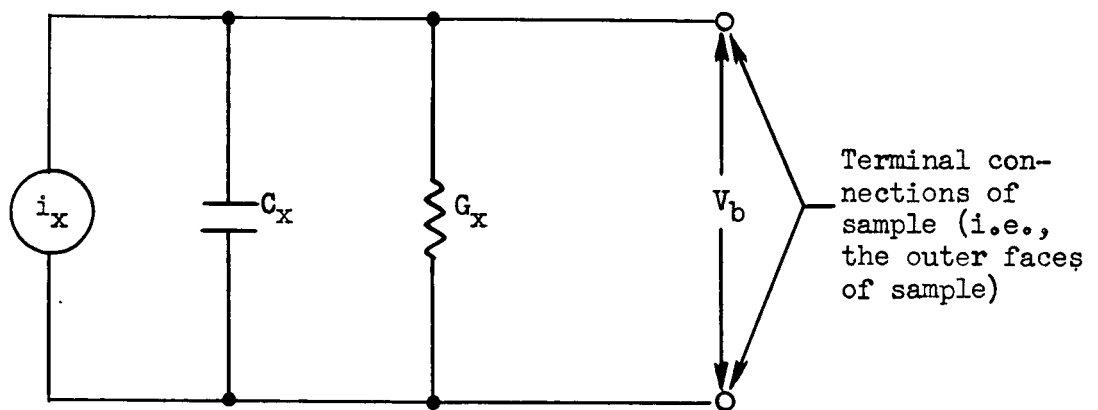


Figure 2. Equivalent circuit of a pyroelectric crystal.

and where a parallel plate configuration has been assumed. The equivalent circuit for equation (1) in terms of an ideal current generator is shown in Figure 2, where the current generator produces a current

$$i_x = A \frac{dP_s}{dT}.$$

If a constant radiation intensity I_0 is modulated sinusoidally so that the intensity striking the sample uniformly is given by the real part of

$$I(t) = \frac{I_0}{2} (1 - e^{j\omega t}), \quad (2)$$

then from Appendix A the steady-state solution for T^* (the temperature of the sample relative to its environment) is

$$T^*(t) = \frac{\alpha I_0}{2B} - \frac{\alpha I_0}{2(B + j\omega c_p \rho l)} \exp(j\omega t). \quad (3)$$

The symbols of equation (3) are defined in Appendix A. The transients have a time constant equal to $c_p \rho l / B$. From equation (3) the time average temperature of the sample relative to its surroundings is

$$T^*_a = (\alpha I_0) / (2B). \quad (4)$$

Differentiating equation (3) and using the definition for i_x gives

$$i_x = A \frac{dP_s}{dT} \frac{\alpha I_0}{2(B + j\omega c_p \rho l)} \exp j(\omega t - \pi/2). \quad (5)$$

Thus i_x is a sinusoidal current with amplitude

$$I_0 = (A \frac{dP_s}{dT} \alpha I_0) / (2 |B + j c_p \rho l|). \quad (6)$$

Putting a capacitive impedance across the output of the detector (see Figure 3) gives a sinusoidal signal voltage across the external impedance whose amplitude is given by

$$V_{so} = \frac{\mathcal{I}_o}{G + j\omega C}, \quad (7)$$

where

$$G = G_e + G_x$$

$$C = C_e + C_x.$$

Using equation (7) and the definition for responsivity R gives

$$R = \frac{V_{so}}{\mathcal{I}_o A} = \frac{\omega a \frac{dP_s}{dT}}{(2|B + j\omega c_p \rho \ell|)(|G + j\omega C|)}. \quad (8)$$

The Johnson noise voltage will be

$$V_n = \frac{\sqrt{4kT\Delta f G}}{G + j\omega C}, \quad (9)$$

and from equations (8) and (9), the NEP is given approximately by

$$NEP \doteq \frac{V_n}{R(\Delta f)^{\frac{1}{2}}} = \frac{2\sqrt{4kT\Delta f G}|B + j\omega c_p \rho \ell|}{\frac{dP_s}{dT} \omega a} \quad (10a)$$

or

$$NEP = \frac{2 c_p \rho \ell}{a \frac{dP_s}{dT}} \sqrt{4kTG} \left| \frac{B}{\omega c_p \rho \ell} + j \right|. \quad (10b)$$

From equation (10) and the definition of specific detectivity D^* ,

one has

$$D^* = (NEP)^{-1} (A)^{\frac{1}{2}} = \frac{a \frac{dP_s}{dT} \sqrt{A}}{2 \sqrt{4kTG} |B + j\omega c_p \rho \ell|}. \quad (11)$$

Typical experimental values for $(B/c_p \rho l)$ have been

$$0.2 \text{ sec}^{-1} \leq B/(c_p \rho l) \leq 2 \text{ sec}^{-1}. \quad (12)$$

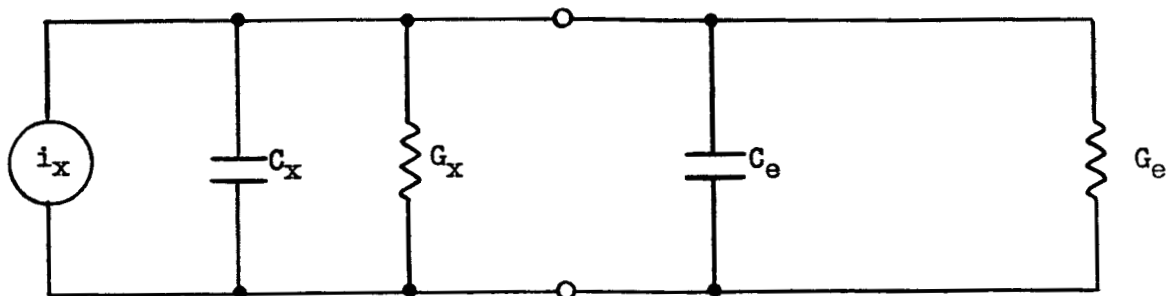


Figure 3. Equivalent circuit of pyroelectric detector with capacitive external impedance.

It therefore follows that for $\omega \geq 20 \text{ sec}^{-1}$, very good approximations to NEP and D^* are

$$\text{NEP} = 2 c_p \rho l \sqrt{4kTG} \left(\alpha \frac{dP_s}{dT} \right)^{-1} \text{ and} \quad (13a)$$

$$D^* = \frac{\alpha \frac{dP_s}{dT} \sqrt{A}}{2 c_p \rho l \sqrt{4kTG}} \quad (13b)$$

respectively.

Limitation on Incident Intensity

Using the typical values for BaTiO_3 detectors constructed thus far in this laboratory, namely

$$B/(c_p \rho l) = 1 \text{ sec}^{-1}$$

$$\begin{aligned} c_p &= 0.5 \text{ joule gm}^{-1} \text{ } ^\circ\text{C}^{-1} \\ \rho &= 6.0 \text{ gm cm}^{-3} \\ l &= 5(10)^{-3} \text{ cm,} \end{aligned}$$

it is found from equation (4) that the average elevation of temperature above room temperature per unit incident intensity is

$$\frac{T_a^*}{I_0 \alpha} = \frac{1}{2B} = 33^\circ\text{C watt}^{-1}\text{cm}^2. \quad (14)$$

Therefore, if a BaTiO_3 crystal is being used at room temperature (20°C), the intensity required to raise its temperature to the Curie point (120°C) is

$$\alpha I_0 \geq (120^\circ\text{C} - 20^\circ\text{C}) / (33^\circ\text{C watt}^{-1}\text{cm}^2) = 3 \text{ watt cm}^{-2}.$$

The result indicates that such detectors can be utilized even with very intense radiation sources, since pyroelectric detectors can be fabricated with very small areas, thus intercepting a small fraction of the radiation from the source. Intense sources (e.g. lasers) are usually pulse devices, and the limitation given here is calculated for a modulated cw source of radiation. Much higher pulse intensities can be tolerated, depending on the pulse duration and relative areas of the beam cross section and the detector.

Thermal Limitation of D^*

If it is assumed that the conductance of the external impedance is zero, the dependence of D^* on sample geometry becomes rather simple. Thus, using

$$G_x = \frac{\omega A \epsilon''}{\ell} \tan \delta \quad (15)$$

and

$$G_e = 0,$$

equation (11) becomes

$$D^* = \frac{\alpha \frac{dP_s}{dT} \omega \sqrt{\ell}}{2 \sqrt{4kT} \omega \epsilon' \tan \delta \left| B + j \omega c_p \rho \ell \right|}. \quad (16)$$

When B is negligible it is seen that reducing the thickness improves D^* , whereas as soon as B dominates, such a reduction has an undesirable effect. Calculated values have served to illustrate clearly that concern must be given to reducing the value of B. The sequence of calculations was made as follows: 1) If B is negligible, D^* becomes

$$D^* \doteq D_1^* = \left[\frac{\alpha \frac{dP_s}{dT}}{\rho c_p \sqrt{\epsilon' \tan \delta}} \right] \left[\frac{1}{2 \sqrt{4kT} \ell \omega} \right]. \quad (17)$$

2) If B dominates, then

$$D^* = D_2^* = \frac{\alpha \frac{dP_s}{dT} \sqrt{\omega \ell}}{2B \sqrt{4kT} \epsilon' \tan \delta}. \quad (18)$$

Therefore the true D^* must lie between D_1^* and D_2^* and the smaller of D_1^* and D_2^* will be a good approximation to D^* .

The results of calculations made from equations (17) and (18) appear in Table I. The first two calculations are for a currently typical thickness of 5×10^{-3} cm and for two values of B that represent the end points of the range of experimental values utilized to date. In these cases, B is dominant and $D^* = D_2^*$. The third entry of Table II was obtained by adjusting the thickness of the sample to make $D_1^* = 3 \times 10^9$ (a value chosen as a goal in future efforts). In this case, it is seen that D_2^* is reduced, indicating that B is

still dominant. The final entry gives the thickness and value of B necessary to achieve a D^* of 3×10^9 .

In all the calculations of Table I typical values of BaTiO_3 single crystals have been utilized, viz.

$$\begin{aligned}\epsilon' &= 300 \epsilon_0 \\ \tan \delta &= 1 \\ \frac{dP_s}{dT} &= 2.5 \times 10^{-8} \text{ coul cm}^{-2} \text{ } ^\circ\text{C}^{-1} \\ c_p &= 0.5 \text{ joule gm}^{-1} \text{ } ^\circ\text{C} \\ \rho &= 6.0 \text{ gm cm}^{-3},\end{aligned}$$

and the absorption coefficient α was assumed to be unity. These calculations are intended as a guide only; they will vary with materials. They serve to point out the dependence of D^* on the sample thickness and effective thermal conductance.

TABLE I
EFFECT OF THICKNESS AND EFFECTIVE THERMAL CONDUCTANCE ON DETECTIVITY D^*
IN BaTiO_3 CRYSTALS

	B	D_1^*	D_2^*	D^*
5×10^{-3}	30	8.7×10^7	4.3×10^6	4.3×10^6
5×10^{-3}	3	8.7×10^7	4.3×10^7	4.3×10^7
4.1×10^{-6}	3	3×10^9	2.4×10^7	2.4×10^7
4.1×10^{-6}	1.2×10^{-3}	3×10^9	3×10^9	3×10^9

SQUARE WAVE ANALYSIS

The analytic expressions for $T^*(t)$ and signal voltage when square wave modulation is used is given in Appendix C. The main

features of the square wave analysis of course remain the same as for the sinusoidal analysis. The average value of $T^*(t)$ is still

$$T_a^* = \frac{\alpha I_0}{2B} . \quad (19)$$

Perhaps the most important feature of this analysis is that it predicts various characteristic shapes for the output signal which depend on the relative sizes of RC , $\frac{C_p R l}{B}$ and τ . All of the characteristic shapes have been observed qualitatively. The characteristic signal wave forms are presented in Figure 4.

MATERIALS PREPARATION

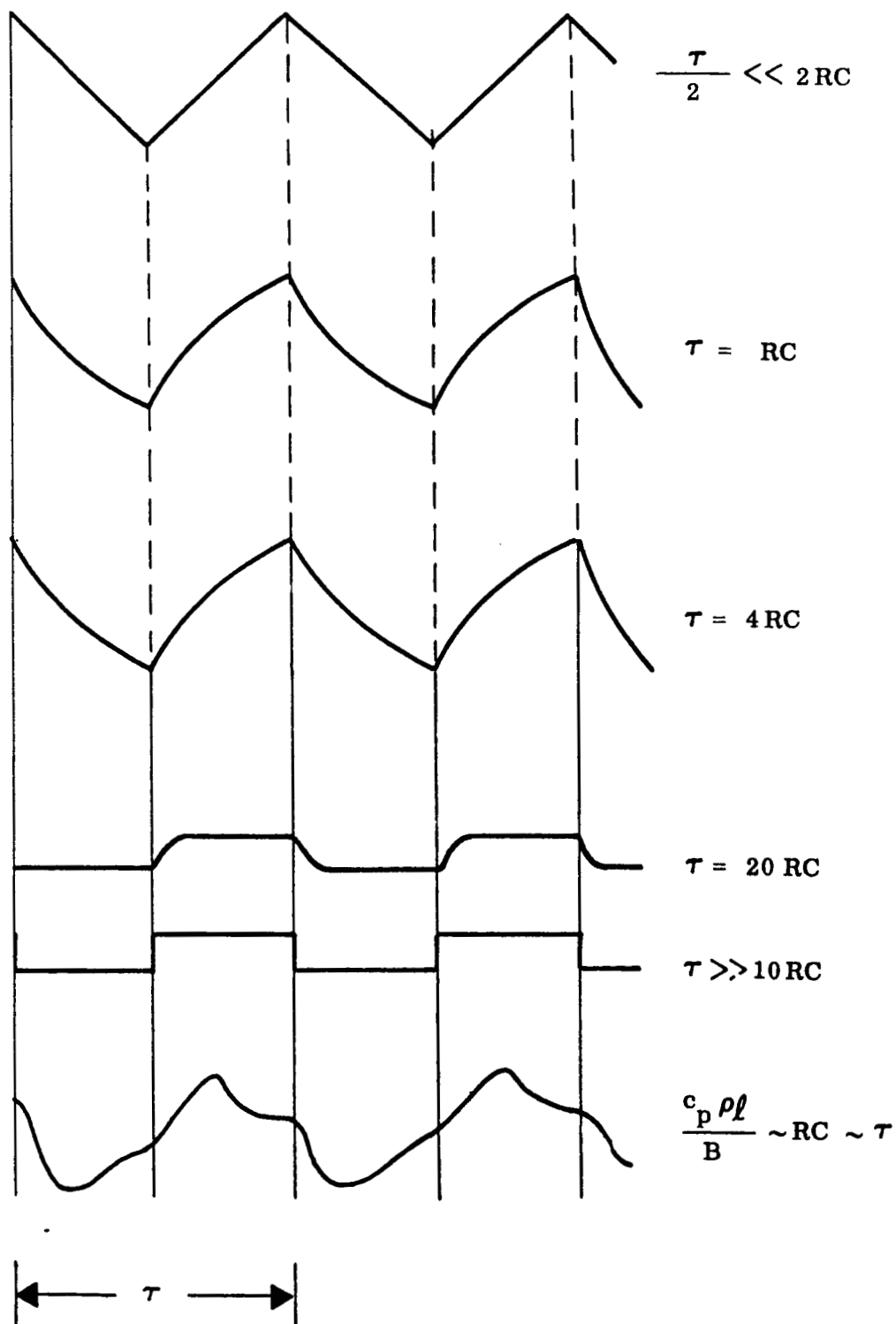
The materials used in the previous reporting period were restricted to single crystal barium titanate, $BaTiO_3$. In this period, most of the measurements continued to concentrate on $BaTiO_3$; however several additional materials were briefly observed. These materials include ceramic $BaTiO_3$ and single crystals of lead titanate, triglycine sulfate, and $BaTiO_3$ doped with iron and yttrium.

Single Crystal Growth

The techniques employed to grow single crystal $BaTiO_3$ were a modified version of the Remeika¹ method in which the crystals are grown from a flux of KF , which is poured off during the cooling portion of the process. Maximum furnace temperature during the firing cycle was $1150^\circ C$. The charge was cooled at about 6 to $25^\circ C/hr$ to $1020^\circ C$, after which it was cooled at furnace rate to room temperature.

¹ J. P. Remeika, J. Am. Chem. Soc. 76, 940(1954).

$$\frac{c_p \rho l}{B} \gg RC$$



828A

Figure 4. Characteristic wave forms observed using square wave modulation.

Single crystals of triglycine sulfate, $(\text{NH}_2\text{CH}_2\text{COOH})_3 \cdot \text{H}_2\text{SO}_4$, have been prepared by growth from aqueous solutions. Glycine and sulfuric acid were dissolved in water to form a saturated solution, from which seed crystals were obtained by allowing the solvent to evaporate. Selected seeds were placed on copper rods and suspended in stirred solutions. Large crystals about one inch on an edge have been prepared using this technique.

Crystals of BaTiO_3 doped with 0.1 mole percent of Y_2O_3 have been grown from the flux and sent to us from the Sperry Rand Research Center, Sudbury, Massachusetts. BaTiO_3 crystals doped with 0.025 percent Fe_2O_3 have been prepared at Clearwater using the Remeika technique previously described.

Preparation and Mounting of Crystals

Crystals of BaTiO_3 to be used as pyroelectric detectors have been prepared according to the following procedure:

The crystals are removed from the crucibles by washing gently with hot water, which dissolves away the KF flux. The crystals are then etched in phosphoric acid at 140-150°C for about a half hour. Sometimes this is followed by poling the crystals using liquid electrodes, after which they are etched at room temperature. This procedure produces clearly visible domain patterns. More frequently, the crystals are washed with deionized water after the high temperature etch. This is followed by a rinse in clean ethyl alcohol and another rinse in deionized water. After the crystals are dried they

are ready for application of electrodes.

The crystals are electroded by evaporation of gold or aluminum onto their surface. This is accomplished in a vacuum by masking all the crystal except the area to be coated. Usually the surface of the crystal is cleaned further by ionic bombardment in the vacuum system. The metal is then evaporated onto one surface of the crystal to a thickness of about 300\AA .

A small square of circuit board is prepared to serve as a mount for the crystal. The board consists of a 1" square of bakelite with Cu strips down the sides as shown in Figure 5. A circular hole is in the center of the board. A 10 mil thick piece of glass onto which two 3000\AA gold strips have been evaporated is attached to the back of the board. The gold strip is connected to the copper strips with aluminum wires as shown in Figure 6. One electroded surface of the crystal is then attached to the gold strips on the glass with silver paste. This configuration is seen in Figure 7. The crystal is then poled by applying liquid electrodes (LiCl and H_2O) on the unplated face of the crystal. The copper strips are grounded and d.c. voltage is applied to the liquid electrode. Fields up to 12,000 to 15,000 v/cm will normally pole a good crystal. The poling process is observed under a microscope using polarized light. When complete polarization is obtained, the liquid electrode is washed off and the crystal is electroded on the remaining surface by vacuum evaporation.

Contact to the top electrode is accomplished by attaching aluminum wire to the electroded surface and the copper strip. The mounted sample can then be clipped into two terminal posts which hold it rigidly in position for measurements. The configuration of the finished sample is shown in Figure 8.

More recently the crystals mounted on boards have been placed in a new holder, designed to permit a rigid mount capable of heating the crystals uniformly to temperatures up to 200°C while measurements of the detector properties are in progress. A description of the mount is given in the next section.

MEASUREMENT APPARATUS

The apparatus used in the measurements for this reporting period was designed and assembled to accomplish the determination of NEP on a variety of pyroelectric crystals at modulation frequencies of 15, 90, 154, and 824 cps using radiation in the optical and near infrared regions. It was further necessary that the temperature of the crystals be capable of continuous variation from ambient to temperatures above 122°C while NEP measurements were made.

These conditions were satisfied by use of the apparatus shown schematically in Figure 9, which is a modification of that used in the earlier reporting period. The source was, for measurements in the optical region, a continuous wave He-Ne laser, radiating at 0.63 microns. For measurements in the infrared region, a black body

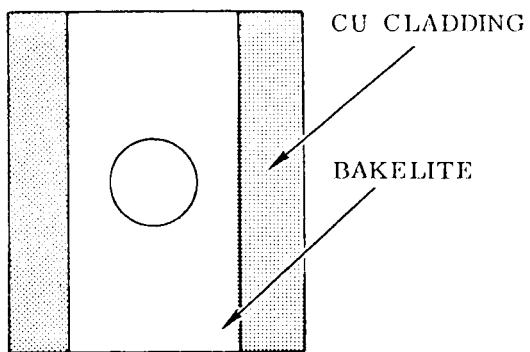


Figure 5
Bakelite Mounting Board

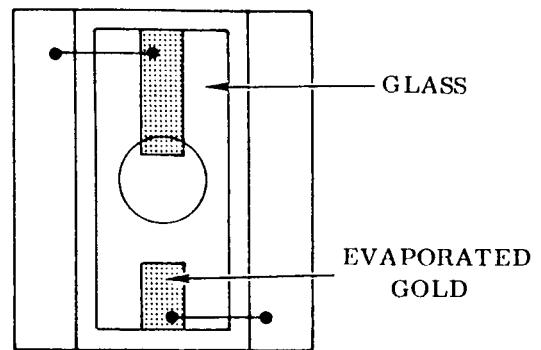


Figure 6
Glass Plate with Conducting
Gold Strips Attached to Mounting
Board

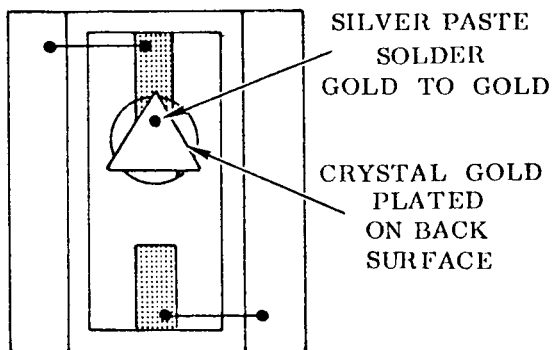
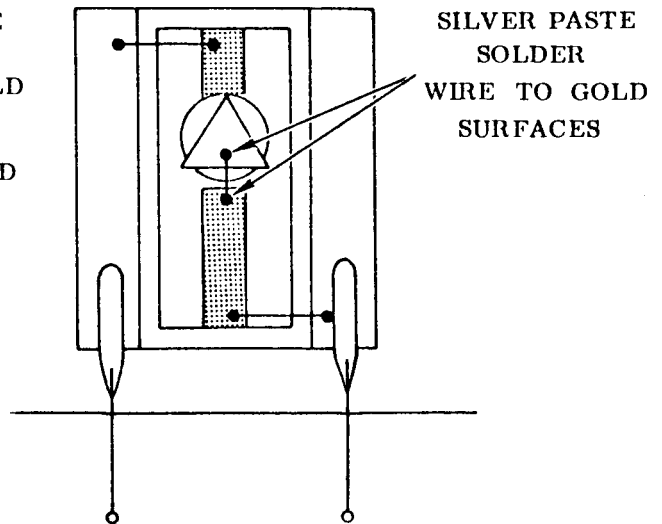


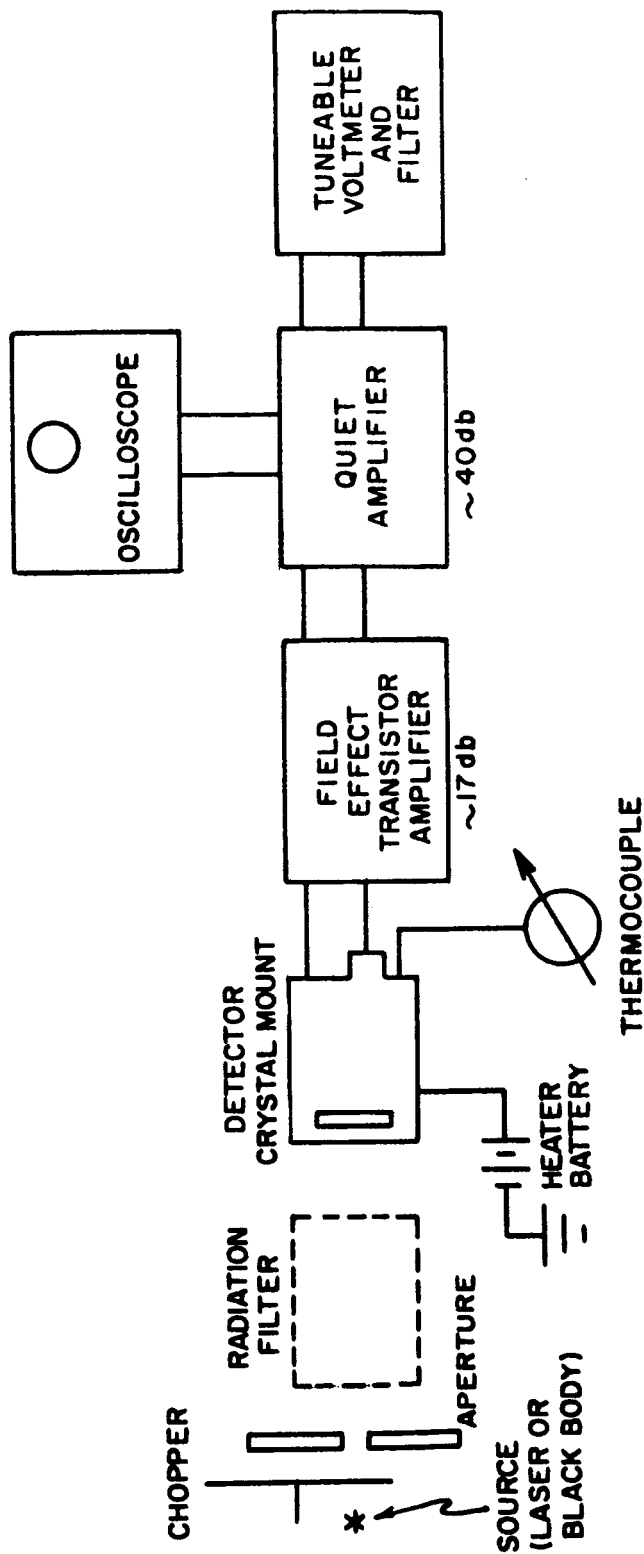
Figure 7
Crystal in Position
for Poling



TO PREAMPLIFIER

Figure 8
Completely Mounted
Crystal

6838



739A

Figure 9. Measurement apparatus for determination of noise equivalent power of a pyroelectric detector.

source at 1000°C was used as a broad source peaked at 2.26 microns and was also used in conjunction with a bandpass filter centered at 3 microns. Earlier plans to include measurements at 15 microns were thwarted because vendors were not able to produce the necessary filter as expected. All modulation was accomplished by mechanical shutters.

The crystal holder is depicted in Figure 10. It is a hollow stainless steel cylinder which stands on an optical bench. It provides a heater coil around the region of the crystal, is monitored by a thermocouple in the same region, and is supplied energy from a storage battery. The preamplifier is required to have low noise and (for use with present BaTiO₃ crystals) a high input impedance. This is effectively accomplished using a field effect transistor in the circuit shown in Figure 11.

The tunable voltmeter is an innovation recently introduced. It consists of a wide range microvoltmeter and a tunable, variable Q filter. The filter is capable of restricting bandwidths to 0.8 cps at a modulating frequency of 15 cps.

Calibration of laser intensity was accomplished by using a Reeder thermopile calibrated against the standard black body source.

EXPERIMENTAL RESULTS

Noise Equivalent Power

A tabulated summary of results of measurements of NEP on typical samples of each variety of crystal is shown in Table II.

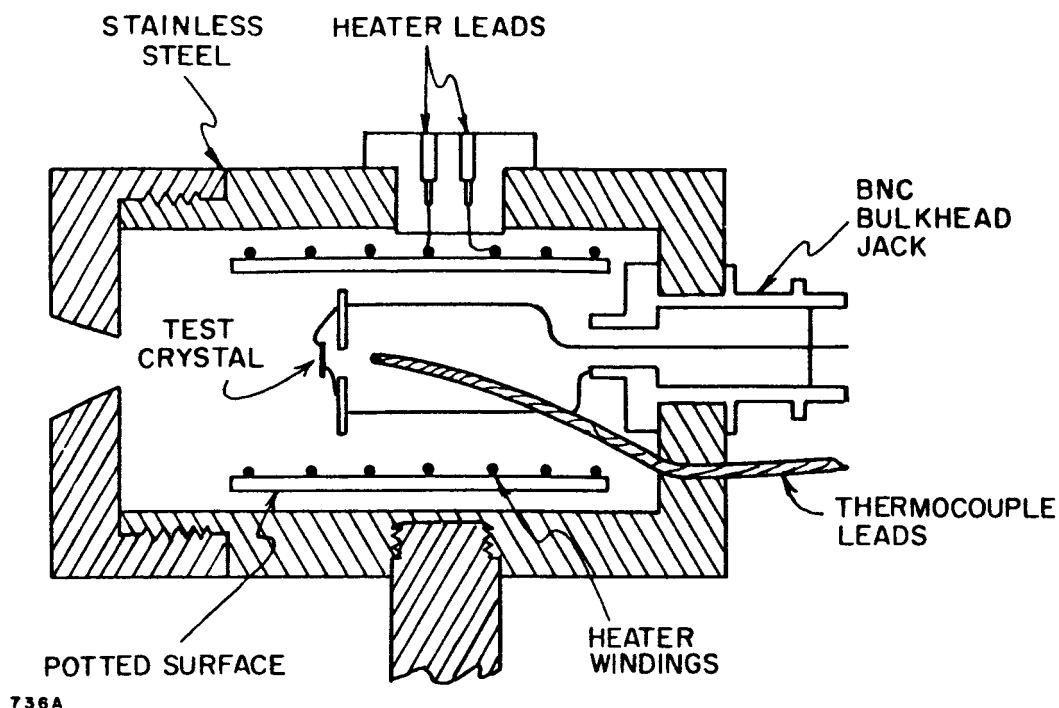


Figure 10. Details of crystal mounted in holder.

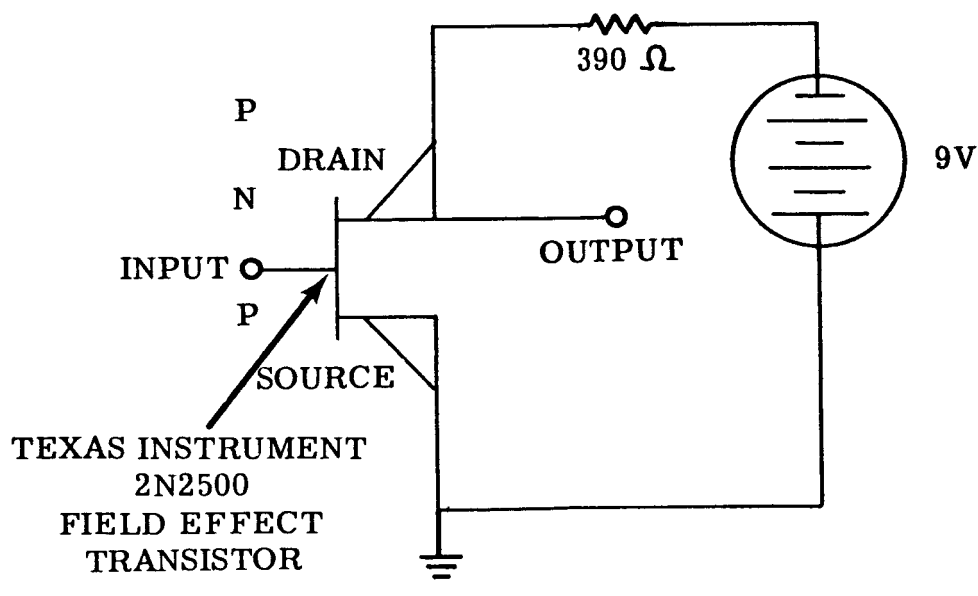


Figure 11. Circuit diagram of preamplifier employing a field effect transistor.

TABLE II
MEASURED NEP AND D* OF PYROELECTRIC MATERIALS*

MODULATION FREQUENCY (CPS)			15			90			154			824		
RADIATION WAVELENGTH (MICRONS)			0.6	2	3	0.6	2	3	0.6	2	3	0.6	2	3
SAMPLE	SAMPLE THICKNESS (CM)	SAMPLE AREA (CM ²)												
BaTiO ₃ S _a -0-10A	9.4x10 ⁻³	5.7x10 ⁻²	6.76(3.6)	3.12(7.7)	2.45(9.8)	76(0.31)	9.5(2.5)	7.0(3.4)	13.6(1.8)	9.4(2.6)	-	19.2(1.3)	25.9(0.93)	-
	8.9x10 ⁻³	3.57x10 ⁻²	22.0(0.86)	8.9(2.1)	6.3(3.0)	320(0.06)	4.7(4.0)	5.25(3.6)	22.0(0.86)	22.8(0.83)	-	28.0(6.8)	9.6(2.0)	-
Doped BaTiO ₃ S _a -0.025-1B (Doped with 0.025 mole per cent Fe ₂ O ₃)	6.4x10 ⁻³	9.25x10 ⁻²	8.0(3.8)	3.0(10.0)	2.45(12.5)	-	6.85(4.4)	4.35(7.0)	-	2.0(15.2)	3.3(9.3)	-	5.5(5.5)	-
	12.7x10 ⁻³	3.57x10 ⁻²	-	3.3(5.8)	1.27(15.0)	-	5.0(3.8)	2.2(8.6)	-	2.4(7.9)	-	-	4.4(4.3)	-
Ceramic BaTiO ₃ Blackened BaTiO ₃ PbTiO ₃ TGS-4	50.8x10 ⁻³	6.46x10 ⁻²	-	139(0.18)	64(0.40)	-	496(0.05)	-	-	388(0.07)	-	-	230(0.11)	-
	2.54x10 ⁻³	5.43x10 ⁻²	-	2.88(8.1)	2.02(11.5)	-	11.9(2.0)	6.9(3.4)	-	-	-	-	-	-
	127.0x10 ⁻³	1.61x10 ⁻²	-	157(0.08)	-	-	-	-	-	-	-	-	-	-
	30.5x10 ⁻³	2.46x10 ⁻²	-	2.8(5.6)	-	-	-	-	-	-	-	-	-	-

* NEP are tabulated in multiples of 10⁻⁸;
D* is given in parentheses in multiples of 10⁶.

On most of the materials, measurements were made at modulating frequencies of 15, 90, 154, and 824 cps, with radiation at 0.63, 2.3, and 3 microns. In some cases, sufficient intensity was not available through the 3 micron filter to permit a measurement. Some of the materials measured at the end of the program were only considered at a single frequency with the black body source.

Excessive values of NEP observed at a modulating frequency of 90 cps were due to 60-cycle contributions to the noise spectrum. Considerable effort was made to minimize pick-up by use of shielding, but with only limited success. NEP measured with the laser at 0.63 microns is not as good as that measured with the black body. This is attributed to the noise associated with the modes of the laser beam, i.e., the continual switching of energy between modes of the laser results in noticeable intensity variation at frequencies up to 1000 cps.

The best value of NEP observed on pure BaTiO₃ was about 3×10^{-8} watts/cps ^{$\frac{1}{2}$} . It was found that blackening of a BaTiO₃ crystal with aquadag produced an improvement in responsivity (and consequently in NEP) of a factor of 30 percent.

The samples of PbTiO₃ tested were prepared from large cubes, about 50 mils on a side. Such configurations are known to be slow in thermal response and the results indicate NEP about 2 orders of magnitude below that of the thin BaTiO₃ samples.

A sample of triglycine sulfate was obtained and measured just prior to the end of this reporting period. Initial measurements

reveal NEP slightly better than BaTiO₃. However the TGS used in this case was not cloven so that the polarization was perpendicular to the crystal face. The responsivity of TGS was strikingly larger than that of BaTiO₃ (see next section).

A few measurements were made to determine the improvement permitted by using lower modulating frequencies. With a BaTiO₃ sample, it was found that a factor of 3.2 improvement in NEP is obtained in going from 15 to 10 cps, the lower limit of the measurement apparatus.

Measurements were made on several samples of ceramic BaTiO₃. These were found to be very insensitive, about two orders of magnitude below the single crystal values. This is assumed to be due to the difficulty in obtaining sufficient polarization in the polycrystalline material. Further investigations of ceramics were omitted in this period.

Responsivity Measurements

Responsivity, the voltage at the crystal per watt of radiation incident on the crystal, is determined from the data observed in measuring the noise equivalent power, provided the gain of the amplifier system is known. The responsivity of all the barium titanate single crystal samples were in the neighborhood of 5 to 10 volts/watt at chopping frequencies of 15 cps, about 1 volt/watt at 90 cps, about 0.5 volts/watt at 154 cps, and about 0.1 volts/watt at 824 cps. No significant difference was observed in materials that were doped.

The triglycine sulfate sample measured showed a larger responsivity at 15cps--200 volts/watt. The noise voltage measured on this sample was somewhat larger than with barium titanate, with the result that the NEP of triglycine sulfate was only moderately better than BaTiO_3 . It is not clear why excess noise attends TGS crystals, and it will be informative to study such crystals that have been cloven carefully and poled as completely as possible.

Temperature Dependence of NEP

The apparatus of Figure 9 was used to study the effects of elevated temperatures on the NEP of BaTiO_3 single crystal detectors. In addition to the apparatus of Figure 9, an X-Y recorder was employed with the thermocouple output providing the X-drive and the tunable voltmeter output supplying the Y-drive. With a fixed bandwidth of the filter and a fixed radiation intensity incident on the crystal, the temperature of the crystal was increased very slowly. The abscissa of the resulting curves are directly proportional to the detectivity of the crystal (detectivity = $1/\text{NEP}$). The result of such a measurement with sample $\text{S}_a\text{-O-10A}$ is shown in Figure 12. Note that the detectivity deteriorates monotonically as the temperature approaches the Curie point (120°C). The noise indicated in the region of the Curie temperature is due to rapidly moving polarization domains which become unbound near the transition and disappear above the Curie point.

The same measurement procedure was carried out again on the same crystal (after re-poling it), except that the preamplifier was removed from the circuit. The preamplifier is a field effect transistor with a capacitive input ($C \approx 50$ pf). The external impedance seen by the crystal is now that of the input to the quiet amplifier, about 8 megohms, resistive. The results of this procedure are shown in Figure 13. Note that the abscissa of the curves of Figures 12 and 13 are not to the same scale.

It is important to point out that the noise voltage was measured from ambient to the Curie temperature and found to be essentially constant, so that it is true that the signal voltage recorded is proportional to the detectivity.

To interpret the results of these measurements, recall the equivalent circuit of the crystal and the external impedance Z_e into which it is connected (see Figure 14). Considering first the case shown in Figure 13, where the external impedance is 8 megohms, the resistance of the crystal R_x is large compared to the external impedance. Even though R_x is decreased with increasing temperature (because the loss tangent of BaTiO_3 increases as the Curie point is approached), the drop across the external impedance is essentially dependent on the current generated. **As stated earlier,** the current is proportional to dP_s/dT , the slope of the spontaneous polarization vs. temperature curves of Figure 15, the signal shown

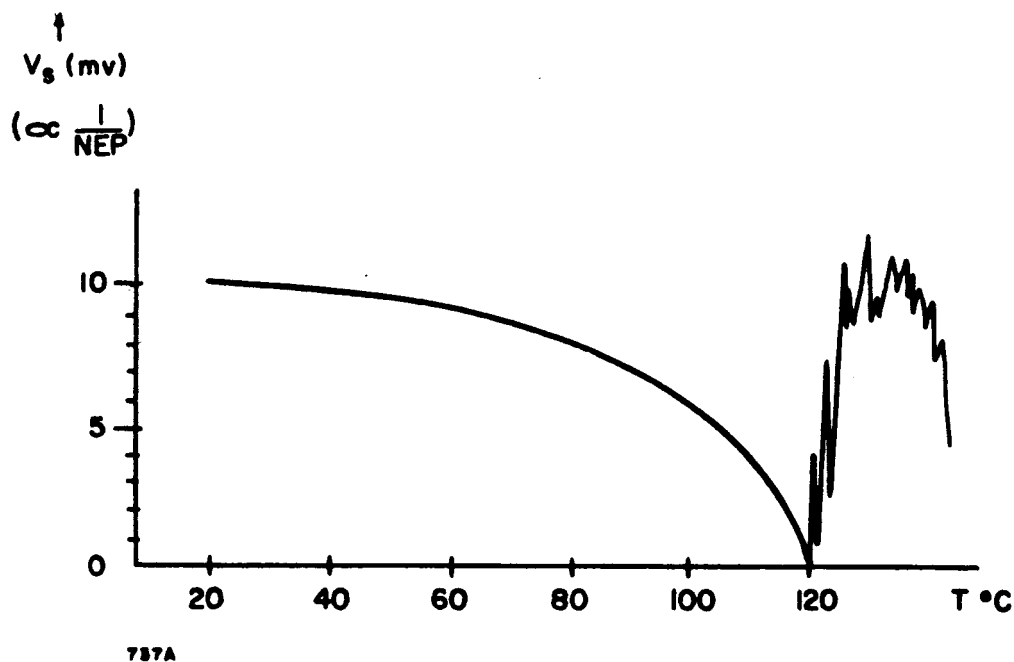


Figure 12. Signal voltage out of pyroelectric detector vs. temperature using capacitive input to preamplifier.

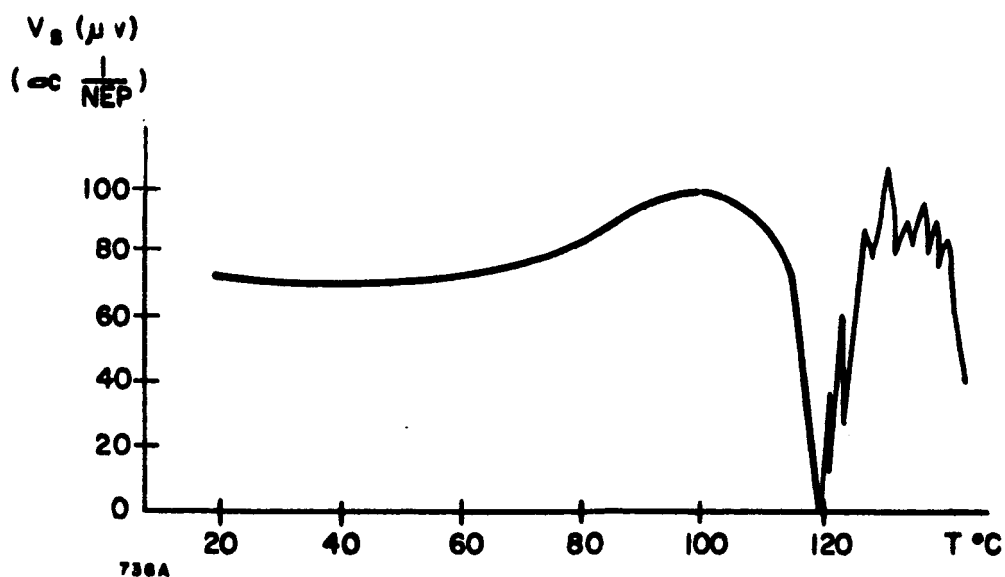
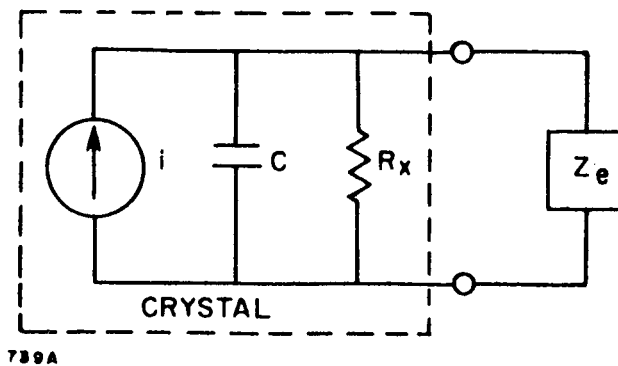
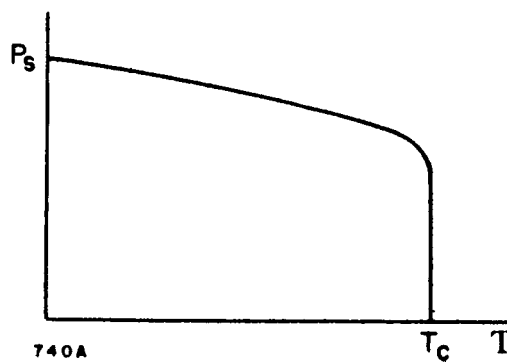


Figure 13. Signal voltage out of pyroelectric detector vs. temperature using resistive input to preamplifier.



739A

Figure 14. Equivalent circuit of pyroelectric detector connected to an external impedance.



740A

Figure 15. Spontaneous polarization vs. temperature for a typical pyroelectric material.

in Figure 13 should increase as the Curie point is approached due to the increased slope of dP_s/dT .

In the case where the external impedance is capacitive, the impedance is large for low modulation frequencies and is therefore comparable to R_x . Thus when R_x is decreased as the Curie point is approached, less and less of the current generated in the crystal is observed as a voltage drop across the preamplifier terminals. This is observed in the curve of Figure 12.

Unfortunately, the NEP measured with the resistive input amplifier is an order of magnitude greater (worse) than with the transistor preamplifier, so that nothing is gained by elevating the sample to temperatures near the Curie point (or, more practically, utilizing a material whose Curie point is only slightly above room temperature). It is seen from Figure 13 however, that no more than 20 percent improvement is obtained in the best case, and such improvement is certainly overshadowed by the prospect of room temperature operation.

Response Time Measurements

Near the end of this reporting period, some brief measurements of response time were made using a $BaTiO_3$ single crystal. Response time was determined as the time required for a square wave modulated incident beam to reach 90 percent of maximum output signal. An oscilloscope was used to measure the response time of a $BaTiO_3$

crystal, which was fed through a transistor preamplifier. To insure the chopped radiation rise time was sufficiently small, a laser beam was focused to a very thin beam and chopped with a wheel whose edges were honed. The speed of the chopping was measured by observing the pulses from a photomultiplier tube. The rise time of the chopped radiation was found to be about 2 microseconds.

Various resistances were placed in parallel with the input of the preamplifier and response time was measured in each case. Of course, the output of the preamplifier was reduced as smaller resistances were used until no signal could be distinguished when a 0.1 megohm resistor was used. The table below shows the rise time measured for typical resistances:

TABLE III

RISE TIMES MEASURED ON BaTiO_3 SINGLE CRYSTALS

Resistance in Parallel with Transistor Preamp	Rise Time (90%)
3.6 Meg	3.0 msec
1.0 Meg	1.0 msec
0.5 Meg	0.5 msec

CONCLUSIONS AND RECOMMENDATIONS

The results of the first phase of this program permit several conclusions, stimulate certain conjectures, and demand that attention be called to certain possible applications for pyroelectric detectors.

The course of the first phase has been that of utilizing the better known pyroelectric materials to determine an accurate analytical model of the detector, while experimental results have justified the models proposed and have provided a basis from which to exploit new and improved materials for specific applications and general improvement of the pyroelectric detector technique.

SUMMARY OF RESULTS

It has been demonstrated that pyroelectric detectors can be accurately characterized by the equivalent circuit shown in Section 4.1 and that the parameters of the materials can be related directly to the detector characteristics. Measurements indicate that the BaTiO_3 crystals several millimeters thick are capable of achieving NEP of about 10^{-8} watt/cps $^{\frac{1}{2}}$. For the area of the crystals measured (0.032 cm^2), this corresponds to a detectivity $D^* \simeq 10^7$. It will be seen in the succeeding sections that such a detector is useful, by virtue of its attendant characteristics (small size, broad frequency range, speed of response, etc.). However, it is desirable that pyroelectric detectors fulfill a more general need, for which greater detectivity is necessary. Searches of the literature indicate that a

detector with broad radiation frequency response, with D^* greater than 10^9 , and having moderate response time would be superior to present uncooled detectors in regions above 6 microns and superior to any operating at liquid nitrogen temperatures (77°K) in regions above 12 microns.

The goal that has been chosen for purposes of calculations is $D^* = 3 \times 10^9$. An earlier section included a discussion of the requirements of materials and their processing for achieving such a goal. A concomitant goal for response time is 1.0 msec, though reduction of D^* will permit faster response.

It is clear that pyroelectric detectors are capable of the broad frequency response characteristic of thermal detectors, and it is reasonable to assume that extremely small detectors can be fabricated as the need arises. The circuitry required to utilize these detectors is simple and standard. Fast response can be achieved in these detectors at the expense of detectivity. Detectors made of BaTiO_3 will be capable of operation when exposed to constant radiation intensities of about 3 watts/cm², and those materials with higher Curie points (e.g., PbTiO_3) will be capable of withstanding cw intensities of 10 watts/cm² or more. Such detectors will be useful in the instrumentation of high energy pulse sources of radiation (e.g., lasers), for in those cases the average power per unit area incident on the detector crystal can be diminished by control of pulse width,

pulse repetition rate, and the relative areas of the pulsed beam and the detector element.

APPLICATIONS OF THE PYROELECTRIC TECHNIQUE

The features of the pyroelectric technique that set it apart from more conventional methods are its relative independence of wavelength of radiation, ambient temperature operation, small physical size, and the relatively short response time compared to other broadband detectors. Assuming that the suggested goals of the next phase of this program are achieved or closely approached, the pyroelectric detector will find extensive use in the far infrared region. It is appropriate to point out that in the near IR region (up to 5 microns), the requirements of most applications will be met most easily by quantum detectors, and when cryogenic operation is permitted, quantum detectors can be extended somewhat further into the infrared region with superior characteristics. Therefore, the applications considered here are restricted to those cases in which the pyroelectric detector may be expected to excel.

Specific Applications

The pyroelectric detector has been found to be of considerable interest for use in certain specific applications, and in many cases it was found to be uniquely adapted to several measurement problems of immediate interest.

Measurements of temperature change in the vicinity of shock tube models appear to be a problem especially suited to pyroelectric

detectors. Changes of temperature of about 50°C occur behind shock model heads in periods of time of the order of hundreds of microseconds. Small, fast response detectors will permit measurement of the temperature change at several positions around the head simultaneously. The shock tube technique requires destruction of the detector element; this implies the desirability of simple, relatively inexpensive detector elements. Pyroelectric detectors seem to be the only detectors that simultaneously satisfy all these requirements.

The measurement of temperature in continuous-flow wind tunnels requires the insertion of a detector into the airstream for sufficiently short periods that laminar flow is not appreciably disturbed. The temperature measured by such a detector is referred to as the "jerk temperature". The requirement here is for a small, fast response, thermal sensor, and the pyroelectric detector will meet all these requirements.

The measurement of the spacial profiles of laser beams that are contained over great distances has apparently been a problem due to the size (and therefore resolution) of ordinary detectors. A simple linear array of pyroelectric detectors has been suggested as a means of accomplishing such measurements. Neither sensitivity nor speed of response appears to be of particular consequence in this application.

Laser instrumentation applications include time profiles of laser pulses obtained by use of pyroelectric techniques. In these cases, the pyroelectric technique is applicable to the optical, near

IR, and far IR regions. Sensitivity is not critical in detecting pulsed laser beams and detectivities of the order of $D^* = 10^5$ are sufficient. Response times for such application, however, should not exceed 0.1 microsecond.

The capability of response to microwave and submillimeter wave signals in a small thermal element is a requirement of groups studying focused beam antenna patterns. Unsuccessful attempts to resolve the focal point of the microwave beam have pointed up the requirement of a small detector with a wide dynamic range. Measurements made in Sperry's laboratories have indicated that pyroelectric detectors may provide the means of solving this problem.

Long Wavelength Applications

The capabilities of pyroelectrics in the long wavelength region of the far infrared will find use in several areas: horizon sensing, infrared imaging, submillimeter wave detection, microwave monitoring, and a group of specialized applications that includes measurement of planetary temperatures, temperature distribution studies, and medical diagnostic techniques.

Current horizon sensors utilize thermal detectors to take advantage of the entire spectrum of radiation from planetary bodies. The realization of pyroelectric detectors with $D^* = 3 \times 10^9$ will provide the most sensitive wide range sensor available, capable of utilizing present scan systems that scan 20 times per second.

Infrared imaging and the utilization of infrared detector arrays have been confronted with several problems: the cooling of arrays and imaging mosaics is nearly impossible in operational systems; physical size of arrays (and therefore of each detector element) must be kept small; obtaining matched elements in arrays is prohibitively expensive and time-consuming. These problems, coupled with the apparent trend toward operation of imaging devices into the far infrared region suggest the possibility of using the small size, ambient temperature operation, and long wavelength capabilities of pyroelectric detectors in this area.

The microwave and submillimeter wave industry have exhibited a tendency to pursue the regions of higher and higher frequencies in an effort to bridge the gap between infrared and microwave technologies. Sensitive pyroelectric detectors in the form of laboratory detectors will fill this pressing need as such studies progress.

RECOMMENDATIONS

In view of the presently existing needs for a sensitive, broadband detector in the far infrared and submillimeter wave regions, and in anticipation of even more serious needs as the electromagnetic spectrum is more completely utilized, it appears especially desirable to develop the pyroelectric detection technique to its fullest extent. The qualities which are of particular interest, it seems, can be listed as follows:

Broad spectral response

Detectivity $\approx 1 \times 10^9$

Small physical size

Fast response time

Reproducibility

It is recommended that these objectives be pursued by the following routes:

- 1) Materials research and improvement
- 2) Theoretical studies of fundamental properties of pyroelectric materials
- 3) Improved processing, mounting, electroding, etc.
- 4) Improved circuitry to utilize the pyroelectric properties.

The parameters affecting pyroelectric characteristics have been demonstrated. Significant improvements can be expected from a thorough investigation of materials properties as they are known to exist and of the means by which they can be improved through doping, growth techniques, and poling. Such studies are first in order of necessity to accomplish the goals of this and similar detector programs.

A parallel study of fundamental processes that contribute to the parameters that govern pyroelectric phenomena is strongly recommended. In particular, the contribution of impurity and lattice defects to the loss character of pyroelectric materials, and the influence of domain dynamics on the pyroelectric efficiency are of especial interest in view of the observation of "hot spots" in materials during the course of this phase of the program.

The processing of materials for use as pyroelectric detectors is, of course, a necessary requirement for their effective utilization. Poling, mounting, electroding, miniaturization, thin film deposition of pyroelectric material, and shielding are some of the areas which must be pursued in conjunction with the materials studies. Effective circuitry must continue to be developed for the detector as the more fundamental studies are pursued.

APPENDIX A

SOLUTION OF HEAT EQUATION FOR SINUSOIDAL MODULATION

If the primary loss of heat from the sample is by conduction to its surroundings, the rate of heat loss will be proportional to the difference in temperature T^* between the sample and its environment. Thus one may write

$$\alpha I A = c_p \rho A \ell \frac{dT^*}{dt} + B A T^*, \quad (1)$$

where

c_p is the specific heat of the sample under constant pressure,

ρ is the density of the sample,

α is the fraction of incident energy absorbed,

I is the intensity of radiation incident upon the sample,

BA is the effective thermal conductance,

A is the area of the sample.

It is now assumed that the intensity is modulated such that

$$I = \frac{I_0}{2} (1 - e^{j\omega t}), \quad (2)$$

where only the real part is physically meaningful. Substituting equation (2) into equation (1) and solving gives

$$T^*(t) = \frac{I_0}{2} \frac{\alpha}{B} \left(1 - e^{-\frac{B}{c_p \rho \ell} t} \right) + \frac{\alpha I_0}{2(B + j\omega c_p \rho \ell)} \left(e^{-\frac{B}{c_p \rho \ell} t} - e^{j\omega t} \right). \quad (3)$$

From equation (3), the time varying steady-state solution is

$$T_s^*(t) = \frac{aI_o}{2B} - \frac{aI_o \exp(j\omega t)}{2(B+j\omega c_p \rho l)} . \quad (4)$$

APPENDIX B

T*(t) FOR SQUARE WAVE MODULATION

The differential equation being used to approximate T*(t) is

$$\frac{dT^*}{dt} + \frac{B}{c_p \rho l} T^* = \frac{B}{c_p \rho l} I(t). \quad (1)$$

Let I(t) be given by

$$I(t) = \begin{cases} I_0 & \text{for } 0 < t < \tau/2 \\ 0 & \text{for } \tau/2 < t < \tau \\ I(t) = I(t - \tau) & \text{for } \tau < t. \end{cases} \quad (2)$$

Using equation (2) and solving equation (1) by Laplace transforms gives the following results.

$$T^*(t) = T_s^*(t) + T_t^*(t) \quad (3)$$

where $T_s^*(t)$ represents the steady state solution and $T_t^*(t)$ represents the transient solution. The explicit form of the two is

$$T_s^*(t) = \begin{cases} \frac{\alpha I_0}{2B} + f(t), & 0 \leq t \leq \tau/2 \\ \frac{\alpha I_0}{2B} - f(t - \tau/2), & \tau/2 \leq t \leq \tau \\ T_s^*(t) = T_s^*(t - \tau), & \tau \leq t, \end{cases} \quad (4)$$

where

$$f(t) = \frac{\alpha I_0}{2B} \left[1 - \frac{2 \exp(-B t / c_p \rho l)}{1 + \exp(B \tau / 2 c_p \rho l)} \right] \quad (5)$$

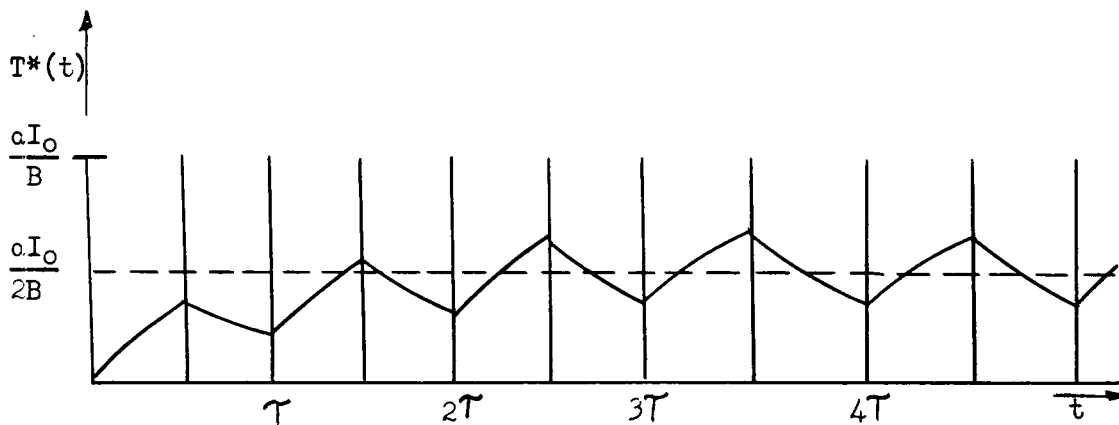
and

$$T_t^*(t) = -\frac{\alpha I_0}{B} \left[\frac{\exp(-B t / c_p \rho l)}{1 + \exp(B \tau / 2 c_p \rho l)} \right], \text{ for all } t > 0. \quad (6)$$

It should be noted that the average value of $T_s^*(t)$ is

$$T_a^* = \frac{\alpha I_o}{2B}. \quad (7)$$

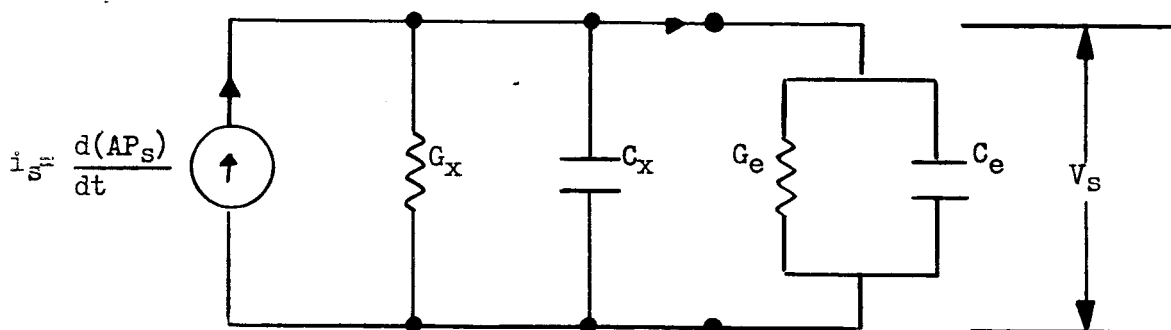
A typical plot of $T^*(t)$ vs. t is given below.



APPENDIX C

SIGNAL VOLTAGE FOR SQUARE WAVE MODULATION

Consider the current generator representation for the equivalent circuit (see Figure) and assume a capacitive external impedance as illustrated.



Then

$$i = -V_s G_e - C_e \frac{dV_s}{dt}, \quad (1)$$

and from equation (1) of Section 4.1 and equation (1) above, one obtains

$$GV_s + \frac{d}{dt} (CV_s + AP_s) = 0, \quad (2)$$

where

$$G = G_e + G_s = 1/R \quad (3a)$$

$$C = C_e + C_s. \quad (3b)$$

Equation (2) can be written in the form

$$\frac{dV_b}{dt} + \frac{1}{RC} V_b = -\frac{A}{C} \frac{dP_s}{dT} \frac{dT}{dt} . \quad (4)$$

Using the fact that

$$\frac{dT^*}{dt} = \frac{dT}{dt}$$

for constant ambient temperature, and differentiating $T^*(t)$ as given in Appendix A, the result can be substituted into equation (4). Solving the resulting equation by Laplace transforms gives

$$V_s(t) = V_{ss}(t) + V_{st}(t) \quad (5)$$

where V_{ss} and V_{st} are the steady-state and transient solutions respectively and are given by

$$V_{ss}(t) = \begin{cases} g(t) & \text{for } 0 \leq t \leq \tau/2 \\ -g(t - \tau/2) & \text{for } \tau/2 \leq t \leq \tau \\ V_{ss}(t) = V_{ss}(t - \tau) & \text{for } \tau < t, \end{cases} \quad (6)$$

$$V_{st}(t) = -g(t) \text{ for all } t > 0, \quad (7)$$

$$g(t) = \left(\frac{\alpha I_o R A}{c_p \rho \ell - B R C} \right) \left(\frac{dP_s}{dT} \right) \left[\frac{\exp(-t/RC)}{1 + \exp(-\tau/2 RC)} - \frac{\exp(-tB/c_p \rho \ell)}{1 + \exp(-B/2c_p \rho \ell)} \right]. \quad (8)$$

If it is assumed that $B = 0$ and $RC \gg \tau$, then one obtains

$$g(t) = \left(\frac{\alpha I_o A}{2c_p \rho \ell C} \right) \left(\frac{dP_s}{dT} \right) \left(\frac{\tau}{4} - t \right). \quad (9)$$

From equation (9), the maximum value of $V_{ss}(t)$ is given by

$$V_o = \frac{\pi \alpha I_o A}{4 c_p \rho \ell c \omega} \left(\frac{dP_s}{dT} \right), \quad (10)$$

where the period τ has been expressed in terms of the angular frequency, i.e.,

$$\tau = 2\pi/\omega. \quad (11)$$

This is to be compared with V_o for sinusoidal modulation under similar restrictions,

$$V_o = \frac{1}{2} \frac{\alpha I_o A}{c_p \rho \ell c \omega} \left(\frac{dP_s}{dT} \right). \quad (12)$$

Typical wave forms as given by equation (6) were depicted in Figure 4 of the text.